

Phase Characterization, Thermal Stability, High-Temperature Transport Properties, and Electronic Structure of Rare-Earth Zintl Phosphides $\text{Eu}_3\text{M}_2\text{P}_4$ ($\text{M} = \text{Ga}, \text{In}$)

Tanghong Yi,[†] Gaigong Zhang,[‡] Naohito Tsujii,^{†,§} Jean-Pierre Fleurial,^{||} Alex Zevalkin,[⊥] G. Jeffrey Snyder,[⊥] Niels Grønbech-Jensen,[‡] and Susan M. Kauzlarich^{*,†}

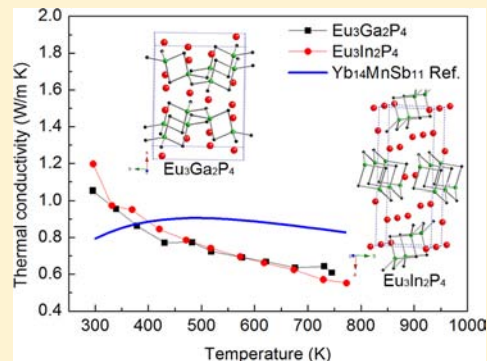
[†]Department of Chemistry and [‡]Department of Applied Science, University of California, One Shields Ave, Davis, California 95616, United States

[§]National Institute for Materials Science, 1-2-1- Sengen, Tsukuba, 305-0047, Japan

^{||}Jet Propulsion Laboratory and [⊥]Materials Science Department, California Institute of Technology, 4800 Oak Grove Drive, Pasadena, California 91109, United States

Supporting Information

ABSTRACT: Two rare-earth-containing ternary phosphides, $\text{Eu}_3\text{Ga}_2\text{P}_4$ and $\text{Eu}_3\text{In}_2\text{P}_4$, were synthesized by a two-step solid-state method with stoichiometric amounts of the constitutional elements. Refinements of the powder X-ray diffraction are consistent with the reported single-crystal structure with space group $C2/c$ for $\text{Eu}_3\text{Ga}_2\text{P}_4$ and $Pnmm$ for $\text{Eu}_3\text{In}_2\text{P}_4$. Thermal gravimetry and differential scanning calorimetry (TG-DSC) measurements reveal high thermal stability up to 1273 K. Thermal diffusivity measurements from room temperature to 800 K demonstrate thermal conductivity as low as 0.6 W/m·K for both compounds. Seebeck coefficient measurements from room temperature to 800 K indicate that both compounds are small band gap semiconductors. $\text{Eu}_3\text{Ga}_2\text{P}_4$ shows p-type conductivity and $\text{Eu}_3\text{In}_2\text{P}_4$ p-type conductivity in the temperature range 300–700 K and n-type conductivity above 700 K. Electronic structure calculations result in band gaps of 0.60 and 0.29 eV for $\text{Eu}_3\text{Ga}_2\text{P}_4$ and $\text{Eu}_3\text{In}_2\text{P}_4$, respectively. As expected for a valence precise Zintl phase, electrical resistivity is large, approximately 2600 and 560 $\text{m}\Omega\cdot\text{cm}$ for $\text{Eu}_3\text{Ga}_2\text{P}_4$ and $\text{Eu}_3\text{In}_2\text{P}_4$ at room temperature, respectively. Measurements of transport properties suggest that these Zintl phosphides have potential for being good high-temperature thermoelectric materials with optimization of the charge carrier concentration by appropriate extrinsic dopants.



INTRODUCTION

A resurgence of interest in thermoelectrics began in the mid 1990s when nanostructural engineering was proposed to play a role in enhancing the thermoelectric efficiency, mainly by reducing the thermal conductivity.^{1,2} Zintl phases have been of particular interest as they are prime candidates for providing the “phonon-glass and electron-crystal” characteristics of ideal thermoelectric materials.^{3,4} Extensive research has been performed on some Zintl phases which exhibit high zT , such as $\text{Yb}_{14}\text{MnSb}_{11}$,⁵ YbZn_2Sb_2 ,⁶ and Zn_4Sb_3 ,^{7,8} and materials with the same or similar structure types. Exploring new Zintl phases with potential for thermoelectric applications is as important as improving the thermoelectric properties of known materials.² Materials containing a light element, in particular, are not heavily studied for thermoelectric applications as it is well understood that the strong covalent bonds within such materials lead to high thermal conductivity. We here present two recently discovered Zintl phases, $\text{Eu}_3\text{Ga}_2\text{P}_4$ and $\text{Eu}_3\text{In}_2\text{P}_4$, and show that they have remarkably low thermal conductivity. This is unusual for phosphides and tend to exhibit thermal conductivity in the range above 10 W/m·K.^{9–13} Recently

reported AMXP_2 ($A = \text{Ca}$ and Yb ; $M, X = \text{Zn}, \text{Cu}$, and Mn) layered phosphides show relatively low thermal conductivity (~ 2 W/m·K) with high Seebeck and low electrical resistivity, demonstrating the potential of phosphides for thermoelectric applications.¹⁴ Thus, the low thermal conductivity in these phases provides opportunities for development of new lightweight efficient thermoelectric materials.

A rare-earth phosphide Zintl phase $\text{Eu}_3\text{Ga}_2\text{P}_4$, isostructural with $\text{Ca}_3\text{Al}_2\text{As}_4$,¹⁵ was recently obtained via a self-flux reaction.¹⁶ $\text{Eu}_3\text{Ga}_2\text{P}_4$ has a monoclinic structure with space group, $C2/c$, and 90 K lattice parameters $a = 13.0245(12)$ Å, $b = 10.1167(10)$ Å, $c = 6.5580(6)$ Å, and $\beta = 90.2430(10)^\circ$.¹⁶ $\text{Eu}_3\text{Ga}_2\text{P}_4$ can be viewed as being composed of two tetrahedral GaP_4 edge-shared units $[\text{Ga}_2\text{P}_6]$ which are further corner shared to form two-dimensional layers in the bc plane with Eu^{2+} cations in between, as shown in Figure 1a. In the structure, each Ga_2P_6 dimer is connected via the terminal P, providing the formula $[\text{Ga}_2\text{P}_2\text{P}_{4/2}]^{6-}$. The cations and anionic units overlap in

Received: November 2, 2012

Published: March 21, 2013

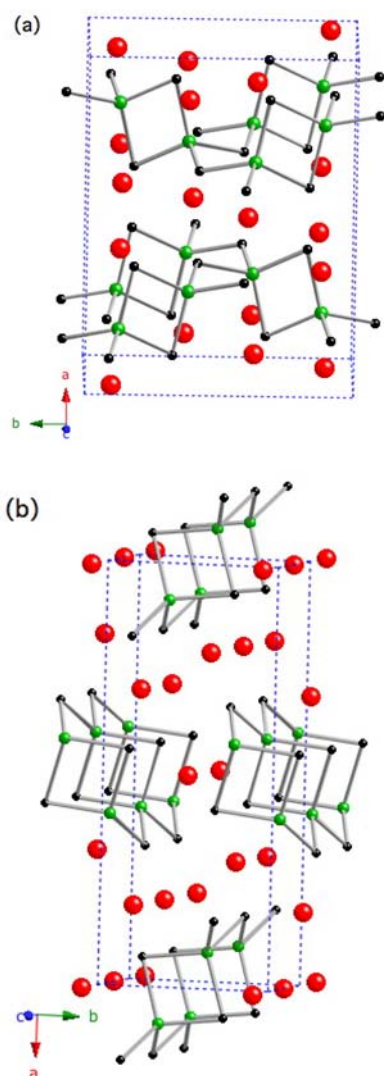


Figure 1. Structures of $\text{Eu}_3\text{Ga}_2\text{P}_4$ (a) and $\text{Eu}_3\text{In}_2\text{P}_4$ (b), with Eu, Ga/In, and P represented by red (large), green (medium), and black (small) spheres, respectively.

the projection of the (110) plane. The phase of $\text{Eu}_3\text{Ga}_2\text{P}_4$ is reminiscent of the isoformula compound $\text{Eu}_3\text{In}_2\text{P}_4$, which crystallizes in an orthorhombic structure (space group $Pnmm$) with 90 K cell parameters $a = 16.097(3)$ Å, $b = 6.6992(13)$ Å, and $c = 4.2712(9)$ Å.¹⁷ $\text{Eu}_3\text{In}_2\text{P}_4$ is isostructural with Zintl phases $\text{Sr}_3\text{In}_2\text{P}_4$ and $\text{Ca}_3\text{In}_2\text{As}_4$ ¹⁸ and structurally related to the $\text{Ca}_3\text{Al}_2\text{As}_4$ ¹⁵ structure type. Each unit composed of edge-shared tetrahedral InP_4 is also corner shared with another two of the same units and stacked to form $[\text{In}_2\text{P}_2\text{P}_{4/2}]^{6-}$ chains along the c axis as shown in Figure 1b. In the $\text{Eu}_3\text{In}_2\text{P}_4$ framework, the two edge-shared tetrahedral units share two terminal P with each other, instead of one as in $\text{Eu}_3\text{Ga}_2\text{P}_4$. Consequently, $[\text{In}_2\text{P}_2\text{P}_{4/2}]^{6-}$ chains are formed in $\text{Eu}_3\text{In}_2\text{P}_4$ rather than the two-dimensional $[\text{Ga}_2\text{P}_2\text{P}_{4/2}]^{6-}$ layers in $\text{Eu}_3\text{Ga}_2\text{P}_4$. Isolated Eu^{2+} cations surround the chains in $\text{Eu}_3\text{In}_2\text{P}_4$. Both of these structure types have been recently described and compared in detail.¹⁹

$\text{Eu}_3\text{Ga}_2\text{P}_4$ and $\text{Eu}_3\text{In}_2\text{P}_4$ were previously reported as single crystals synthesized via flux reaction.^{16,17} Both $\text{Eu}_3\text{Ga}_2\text{P}_4$ and $\text{Eu}_3\text{In}_2\text{P}_4$ were discovered as side products of the flux synthesis of EuGa_2P_2 ²⁰ and Eu_3InP_3 ,^{17,21} respectively. A series of $\text{A}_3\text{Al}_2\text{Pn}_4$ and $\text{A}_3\text{Ga}_2\text{Pn}_4$ ($\text{A} = \text{Ca}, \text{Sr}, \text{Ba}, \text{Eu}; \text{Pn} = \text{P}, \text{As}$)

compounds have recently been explored through flux reaction.¹⁹ However, $\text{Eu}_3\text{Ga}_2\text{P}_4$ was not obtained under the experimental conditions explored in the report. Solid-state reaction with a stoichiometric amount of elements in tantalum tubes was explored in order to prepare $\text{Eu}_3\text{In}_2\text{P}_4$ but was unsuccessful.¹⁷ In the present paper, we report a two-step solid-state reaction method to make phase-pure products of $\text{Eu}_3\text{Ga}_2\text{P}_4$ and $\text{Eu}_3\text{In}_2\text{P}_4$. Phase characterization, thermal stability, transport properties, and electronic structures of both compounds are studied.

EXPERIMENTAL SECTION

Synthesis. Pure elements of Eu (ingot, 99.999%, Ames Lab), Ga (6 mm pellets, 99.9999%, Alfa Aesar), In (3 mm shot, 99.99%, CERAC), and red P (polycrystalline lump, 99.9999%, J. Matthey) were used to prepare $\text{Eu}_3\text{Ga}_2\text{P}_4$ and $\text{Eu}_3\text{In}_2\text{P}_4$. Samples were synthesized using a two-step solid-state reaction method. The first step was to make Eu and Ga/In binary phases by mixing Eu and Ga/In at a ratio of 3/2. Elements were loaded into a Nb tube and sealed by arc welding. The Nb tube was then sealed in a quartz tube under vacuum before being put into a furnace. The reaction was heated in a programmable furnace (Barnstead Thermolyne 4800) under the following temperature profile: for Eu and Ga, heating to 1323 K from room temperature in 6 h, dwelling at 1323 K for 12 h, then cooling to 823 K within 6 h, and dwelling at 823 K for 96 h; for Eu and In, ramping to 1273 K in 6 h, dwelling at 1273 K for 12 h, then cooling to 1023 K in 6 h, dwelling at 1023 K for 24 h, followed by cooling to 923 K in 6 h, and dwelling at 923 K for 72 h. The second step was to add proper amounts of red phosphorus to the ball-milled powders of Eu and Ga/In binary phases in an alumina crucible, which was sealed in a quartz tube under vacuum. The same heating profile was used in both reactions: heating to 473 K in 6 h, then heating to 1073 K in 120 h, followed by dwelling at 1073 K for 12 h. Final products of $\text{Eu}_3\text{Ga}_2\text{P}_4$ and $\text{Eu}_3\text{In}_2\text{P}_4$ powders were obtained by opening the ampule in a nitrogen-filled glovebox.

Both $\text{Eu}_3\text{Ga}_2\text{P}_4$ and $\text{Eu}_3\text{In}_2\text{P}_4$ are air sensitive. $\text{Eu}_3\text{Ga}_2\text{P}_4$ is more air sensitive than $\text{Eu}_3\text{In}_2\text{P}_4$ and turns into a yellowish powder after being exposed in air for several hours. Dense pellets of $\text{Eu}_3\text{Ga}_2\text{P}_4$ and $\text{Eu}_3\text{In}_2\text{P}_4$ from spark plasma sintering (SPS) were less reactive due to the minimized surface area but still crumbled into pieces and powders after several days of being exposed to air.

Powder X-ray Diffraction. Powder of $\text{Eu}_3\text{Ga}_2\text{P}_4$ was loaded in to an airtight holder for powder X-ray diffraction (XRD). A zero-background holder was used for $\text{Eu}_3\text{In}_2\text{P}_4$ in order to get better quality data since this compound is less air sensitive. XRD data were collected by a Bruker D8 diffractometer with $\text{Cu K}\alpha$ radiation ($\lambda = 1.54060$ Å) with a step size of 0.02° and scan rate of 1 s per step. Data acquisition was done using the software with Bruker. Refinements were performed with the FullProf Suite using the profile matching mode.²²

Thermogravimetry and Differential Scanning Calorimetry (TG-DSC). Pellets pressed from the powder of $\text{Eu}_3\text{M}_2\text{P}_4$ ($\text{M} = \text{Ga}, \text{In}$) were used for TG-DSC analysis. Data were obtained with a Netzsch Thermal Analysis STA 409 cell equipped with a TASC 414/2 controller and a PU 1.851.01 power unit. After the baseline was established, a pellet (~ 30 mg) was loaded into an alumina crucible at room temperature, and after purging the sample chamber, the sample was measured under an argon flow at 10 K/min with a data acquisition rate of 10 points/K. Data acquisition was performed using the software provided with the equipment and analyzed with the Netzsch Proteus computer program.

Thermoelectric Property Sample Preparation. Finely ground polycrystalline powders were pressed in high-density graphite dies under 55 MPa up to 1023 K and held for 5 min under vacuum. The density of the pellets was about 98% of the theoretical density. Coin-shaped samples were obtained after spark plasma sintering (SPS) with 12.7 mm diameter and approximately 1.5 mm thickness. Discs for electrical and thermal transport properties measurements were polished down to typically 1 mm thickness with two smooth parallel surfaces.

Transport Properties Measurements. Electrical resistivity (ρ) was measured using the van der Pauw technique with a high-temperature apparatus. The Hall coefficient was also measured in the same apparatus with a constant magnetic field about 9000 G. Carrier density (n) was calculated from the Hall coefficient (R_H) based on $n = 1/R_H e$ assuming a scattering factor of 1.0 in a single-carrier scheme, where n is the charge carrier density, R_H is the Hall coefficient, and e is the charge of the electron. The Hall mobility (μ_H) was calculated from the Hall coefficient (R_H) and the resistivity values according to equation $\mu_H = R_H/\rho$.

Thermal diffusivity was measured using a flash diffusivity technique (LFA457, NETSZCH) with a PyroCeram 9606 standard.²³ Thermal conductivity was calculated according to the equation $\kappa = C_p dD$, where the heat capacity (C_p), geometric density (d), and thermal diffusivity (D) are from experimental data. Thermal diffusivity data are provided in the Supporting Information along with the calculated thermal conductivity.

The Seebeck coefficient was measured using a high-temperature light pulse technique.²⁴ A small auxiliary heater was used to produce a temperature difference ΔT across the sample while simultaneously measuring the thermoelectric voltage ΔV produced across it. The Seebeck coefficient was calculated by the slope of the line of ΔV vs ΔT .

Electronic Structure Calculations. First-principle electronic structure calculations of $\text{Eu}_3\text{Ga}_2\text{P}_4$ and $\text{Eu}_3\text{In}_2\text{P}_4$ were performed based on density functional theory (DFT), in which the exchange correlation potential employed the generalized gradient approximation (GGA) and the functional was given by Perdew, Burke, and Ernzerhof (PBE). Projector-augmented wave (PAW) pseudopotentials were used to model the interaction between valence electrons and core electrons. Through our calculation, the plane wave basis set was determined with an energy cutoff at 337.5 eV for both $\text{Eu}_3\text{Ga}_2\text{P}_4$ and $\text{Eu}_3\text{In}_2\text{P}_4$. Integrations within the Brillouin zone specific K points were selected using a $2 \times 2 \times 2$ Gamma-Centered grid for the $\text{Eu}_3\text{Ga}_2\text{P}_4$ 36-atom supercell and a $4 \times 4 \times 4$ grid for the $\text{Eu}_3\text{In}_2\text{P}_4$ 18-atom supercell calculation.

The partially occupied and strongly correlated localized f orbitals of Eu were treated using the GGA(S) + U method. By explicitly adding the Hubbard on-site Coulomb repulsion U parameter in the energy functional, the excessive delocalization predicted by LDA/GGA could be remedied. Our calculations were performed using Dudarev's approach for GGA(S) + U_{eff} in which $U_{\text{eff}} = U - J = 6.3$ eV,²⁵ and with Europium magnetic moment $7 \mu_B$.²⁶ All calculations were conducted with the Vienna ab initio program package (VASP).

RESULTS AND DISCUSSION

Synthesis and Phase Characterization. Pure phases of monoclinic $\text{Eu}_3\text{Ga}_2\text{P}_4$ and orthorhombic $\text{Eu}_3\text{In}_2\text{P}_4$ were successfully synthesized by means of a two-step solid-state reaction with stoichiometric elements. The titled compounds could not be prepared phase pure by directly melting stoichiometric elements together in one step at temperatures of 1100 °C, with impurity EuP and GaP or InP binary phases and ternary phases being formed. Making Eu_xGa_y or Eu_xIn_y binary phases is a crucial first step, inhibiting formation of binary phosphides and other ternary phases that makes it difficult to synthesize pure $\text{Eu}_3\text{M}_2\text{P}_4$ ($M = \text{Ga}, \text{In}$).^{16,17,21,27}

The powder X-ray diffraction patterns of the two compounds were used to determine the purity of the phase. The whole pattern fitting of the data for both compounds is shown in Figure 2 with agreement R factors $R_{\text{wp}} = 16.1\%$, $R_{\text{exp}} = 10.89$ and $R_{\text{wp}} = 9.15\%$, $R_{\text{exp}} = 5.19\%$ for $\text{Eu}_3\text{Ga}_2\text{P}_4$ and $\text{Eu}_3\text{In}_2\text{P}_4$, respectively. No obvious impurity was detectable by X-ray diffraction based on the Bragg positions and the difference between observed and calculated patterns. The high background at low angle in the diffraction pattern of $\text{Eu}_3\text{Ga}_2\text{P}_4$ was contributed by the airtight holder. Cell parameters were $a =$

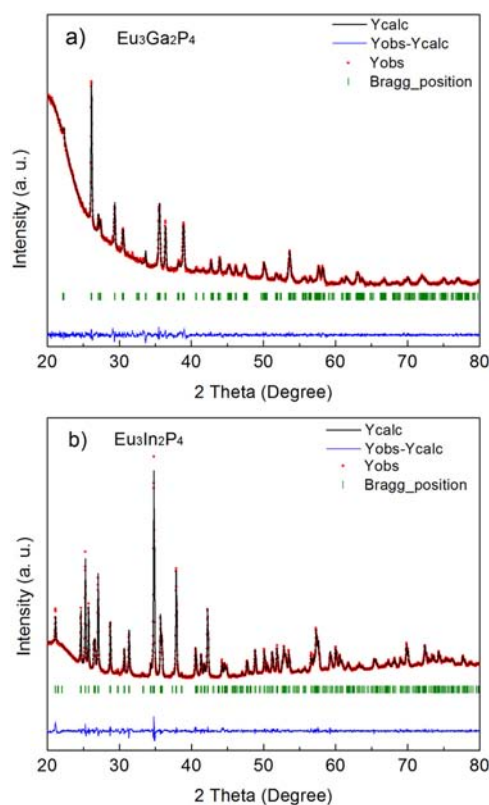


Figure 2. Powder X-ray diffraction pattern of $\text{Eu}_3\text{Ga}_2\text{P}_4$ (a) and $\text{Eu}_3\text{In}_2\text{P}_4$ (b) with data marked as red dots and calculated patterns in black, the difference between experimental and calculated patterns shown in blue, and the Bragg positions indicated as green bars.

$13.0111(4) \text{ \AA}$, $b = 10.1157(2) \text{ \AA}$, $c = 6.5767(2) \text{ \AA}$, and $\beta = 90.066(2)^\circ$ for $\text{Eu}_3\text{Ga}_2\text{P}_4$ and $a = 16.1527(2) \text{ \AA}$, $b = 6.7297(1) \text{ \AA}$, and $c = 4.2769(1) \text{ \AA}$ for $\text{Eu}_3\text{In}_2\text{P}_4$, in good agreement with reported single-crystal data.^{16,17} Pellets of $\text{Eu}_3\text{Ga}_2\text{P}_4$ and $\text{Eu}_3\text{In}_2\text{P}_4$ obtained from SPS had the same X-ray diffraction patterns as the premade powders (not shown).

Thermal Stability. $\text{Eu}_3\text{Ga}_2\text{P}_4$ and $\text{Eu}_3\text{In}_2\text{P}_4$ have no melting behavior below 1273 K according to the TG-DSC analyses in Figure 3. No obvious endothermic or exothermic peaks are observed in the DSC curves for either compound. The continual minor increases in the DSC curves observed in both compounds as a function of temperature is consistent with sintering of the powder during the heating process. The small mass increase upon heating is attributed to slight surface oxidation during data collection. The thermal stability of the two titled compounds makes them applicable as high-temperature thermoelectric materials.

Transport Properties. Both $\text{Eu}_3\text{Ga}_2\text{P}_4$ and $\text{Eu}_3\text{In}_2\text{P}_4$ have extremely low thermal conductivity values. These were calculated from geometric density (d), measured heat capacity (C_p), and thermal diffusivity (D) from flash diffusivity measurement using the equation $\kappa = C_p dD$. Thermal conductivities of the two systems are as low as 0.6 W/m·K, compared with one of the best p-type Zintl phase materials $\text{Yb}_{14}\text{MnSb}_{11}$,⁵ which is about 0.9 W/m·K as shown in Figure 4. However, the lattice thermal conductivity values of both materials are nearly identical, because $\text{Yb}_{14}\text{MnSb}_{11}$ has a significant electronic contribution, κ_e , while in the case of $\text{Eu}_3\text{M}_2\text{P}_4$ ($M = \text{Ga}, \text{In}$), κ_e is negligible due to low electronic conductivity. The thermal conductivity, κ , decreases with

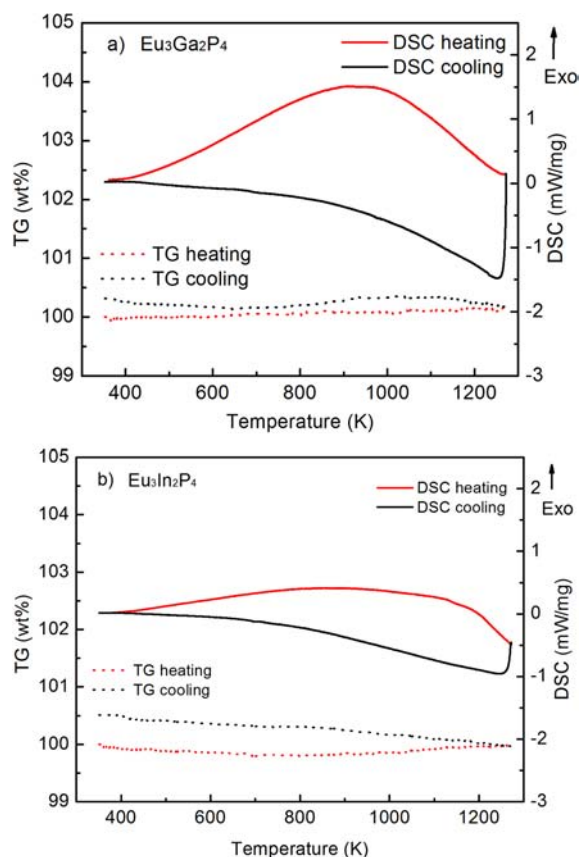


Figure 3. TG-DSC traces for $\text{Eu}_3\text{Ga}_2\text{P}_4$ (a) and $\text{Eu}_3\text{In}_2\text{P}_4$ (b). Solid and dotted curves are for DSC and TG and red and black curves for heating and cooling, respectively.

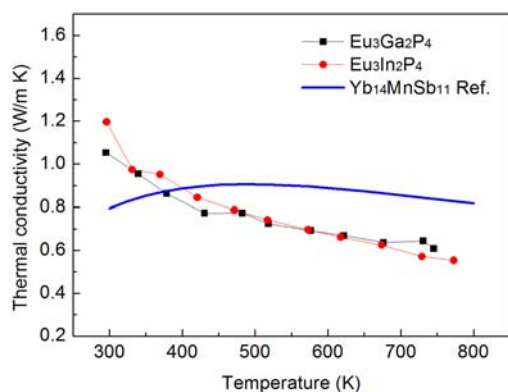


Figure 4. Thermal conductivities of $\text{Eu}_3\text{Ga}_2\text{P}_4$ and $\text{Eu}_3\text{In}_2\text{P}_4$ with $\text{Yb}_{14}\text{MnSb}_{11}$ (solid line) from the literature⁵ for comparison as a function of temperature.

increasing temperature due to the increased phonon Umklapp scattering. In rare-earth Zintl phases such as $\text{Yb}_{14}\text{MnSb}_{11}$ ⁵ and $\text{Yb}_{11}\text{MSb}_9$ ($M = \text{Ga}, \text{In}$),²⁸ heavy atoms in large and complex unit cells lead to extremely low lattice thermal conductivity. It is of interest to achieve extremely low thermal conductivity approaching the glassy limit in relatively light phosphide compounds, such as bulk $\text{Eu}_3\text{Ga}_2\text{P}_4$ and $\text{Eu}_3\text{In}_2\text{P}_4$.²⁹ Low thermal conductivity of Zintl phosphides has recently been observed for AMXP_2 ($A = \text{Ca}$ and Yb ; $M, X = \text{Zn}, \text{Cu}$, and Mn) systems.¹⁴ These Zintl phosphides naturally possess the “phonon glass” property mainly due to the unit cell complexity. With proper dopants to optimize the power factor ($P = S^2\sigma$) by

tuning carrier concentration and/or the density of states near the Fermi level, Zintl phosphides could be promising candidates for approaching ideal “phonon glass, electron crystal” materials.^{4,30}

Figure 5 shows the temperature-dependent electrical resistivity (ρ) of $\text{Eu}_3\text{Ga}_2\text{P}_4$ and $\text{Eu}_3\text{In}_2\text{P}_4$ from room temper-

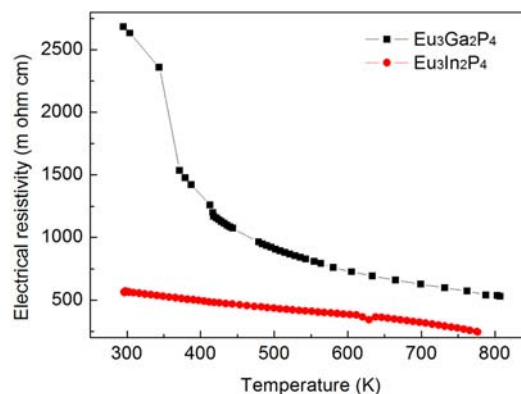


Figure 5. Electrical resistivity of $\text{Eu}_3\text{Ga}_2\text{P}_4$ and $\text{Eu}_3\text{In}_2\text{P}_4$ as a function of temperature.

ature to about 800 K. The decreasing electrical resistivity with increasing temperature indicates that both samples act as semiconductors. $\text{Eu}_3\text{Ga}_2\text{P}_4$ has a much higher electrical resistivity than $\text{Eu}_3\text{In}_2\text{P}_4$, which suggests that $\text{Eu}_3\text{Ga}_2\text{P}_4$ possesses a larger band gap. The room-temperature electrical resistivity of $\text{Eu}_3\text{In}_2\text{P}_4$ is approximately 560 $\text{m}\Omega\cdot\text{cm}$ (0.0056 $\Omega\cdot\text{m}$), which is consistent with the reported value of 0.005(1) $\Omega\cdot\text{m}$ from single crystals.¹⁷ However, the room-temperature ρ of polycrystalline $\text{Eu}_3\text{Ga}_2\text{P}_4$ of this work, approximately 2600 $\text{m}\Omega\cdot\text{cm}$ (0.026 $\Omega\cdot\text{m}$), is 3 orders of magnitude lower than the reported value of about 250 $\Omega\cdot\text{m}$ for a single crystal with a current parallel to the b axis.¹⁶ Data were analyzed by an activation model, $\ln \rho = E_g/2k_B T + A$, shown in Figure 6. Band

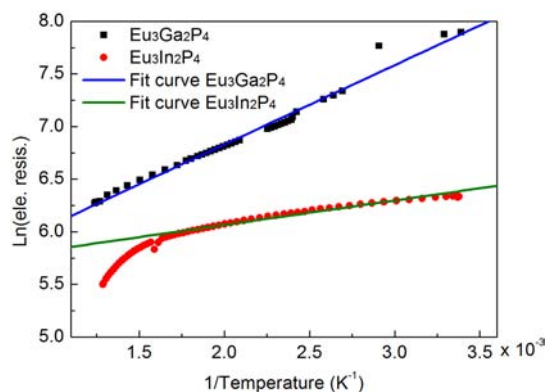


Figure 6. $\ln \rho$ versus $1/T$ and linear fit to the data of $\text{Eu}_3\text{Ga}_2\text{P}_4$ ($T = 380\text{--}800$) and $\text{Eu}_3\text{In}_2\text{P}_4$ ($T = 300\text{--}600$).

gaps, E_g , of 0.120(1) and 0.040(1) eV were obtained for $\text{Eu}_3\text{Ga}_2\text{P}_4$ (300–800 K) and $\text{Eu}_3\text{In}_2\text{P}_4$ (300–600 K), respectively. These values are much smaller than the reported results from single crystals of 0.552(2)¹⁶ (280–300 K) and 0.452(4) eV¹⁷ (130–300 K) for $\text{Eu}_3\text{Ga}_2\text{P}_4$ and $\text{Eu}_3\text{In}_2\text{P}_4$, respectively. The difference may be attributed to the different temperature ranges used for data fitting and the form of the samples (polycrystalline vs single crystalline). Further, as shown

in Figure 6, the two curves do not fit well for a wide temperature range, indicating that the activation model may not be applicable for a wide temperature range in this case, as was also reported for wide temperature range in our previous work on $\text{Eu}_3\text{Ga}_2\text{P}_4$ single crystals.¹⁶ A variable-range-hopping (VRH) model was applied to better fit the experimental data of $\text{Eu}_3\text{Ga}_2\text{P}_4$.¹⁶ The results of the fitting with the VRH model suggested that the carrier conduction in $\text{Eu}_3\text{Ga}_2\text{P}_4$ was mostly three dimensional. In other words, besides the two-dimensional Ga–P networks indicated in Figure 1, Eu–P bonding is also involved in carrier conduction. Eu–P distances in $\text{Eu}_3\text{Ga}_2\text{P}_4$ range from 2.9376 to 2.9961 Å, which are comparable to the ones in $\text{Eu}_3\text{In}_2\text{P}_4$ from 2.9598 to 2.9957 Å. The Eu–P interactions in $\text{Eu}_3\text{M}_2\text{P}_4$ (M = Ga, In) are also shown in the valence charge density contour maps, discussed below.

The Hall carrier concentration (n_{H}) of $\text{Eu}_3\text{Ga}_2\text{P}_4$ is positive, indicating that it is a p-type semiconductor. In $\text{Eu}_3\text{Ga}_2\text{P}_4$, n_{H} increases exponentially with temperature, as shown in Figure 7a, which can be explained by the thermal excitation of carriers

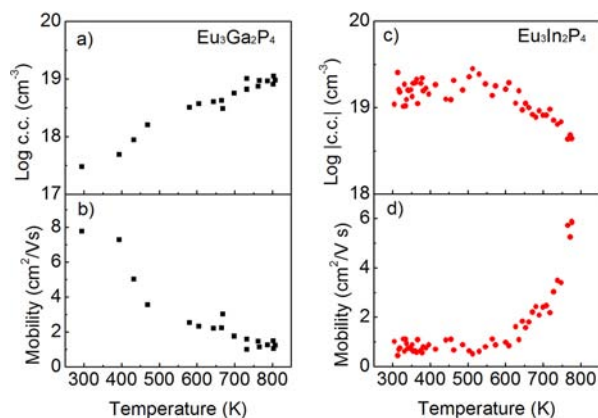


Figure 7. (a) $\text{Eu}_3\text{Ga}_2\text{P}_4$ carrier concentration increases with temperature; (b) mobility decreases with temperature. (c) $\text{Eu}_3\text{In}_2\text{P}_4$ Hall carrier concentration decreases with temperature; (d) Hall mobility increases with temperature. y axis of a and c is $\log(\text{carrier concentration})$. Hall carrier concentration and Hall mobility are calculated according to the single-band approximation. Unusual temperature dependence observed in $\text{Eu}_3\text{In}_2\text{P}_4$ is due to the influence of minority carriers.

across the small band gap. The Hall mobility (μ_{H}) of $\text{Eu}_3\text{Ga}_2\text{P}_4$ decreases with increasing temperature due to the increasing phonon scattering and carrier concentration, shown in Figure 7b. The continuous decrease of the electrical resistivity of $\text{Eu}_3\text{Ga}_2\text{P}_4$ with temperature indicates that the rise of the carrier concentration exceeds the mobility decay. This is typical behavior for an intrinsic semiconductor. However, $\text{Eu}_3\text{In}_2\text{P}_4$ provides a completely different scenario. The Hall charge carrier concentration (n_{H}) of $\text{Eu}_3\text{In}_2\text{P}_4$ is that of an n-type material. The absolute value of the Hall carrier density has no appreciable change up to about 550 K and then decreases with increasing temperature afterward, shown in Figure 7c. The decreasing of Hall carrier density contributes to the appearance of an increasing Hall mobility as shown in Figure 7d. Overall, the electrical resistivity of $\text{Eu}_3\text{In}_2\text{P}_4$ decreases with increasing temperature as shown in Figure 5. The difference in the sign of Seebeck and Hall coefficient, abnormal change of carrier concentration, and temperature dependence of the Seebeck coefficients (shown in Figure 8) for $\text{Eu}_3\text{In}_2\text{P}_4$ taken together are consistent with the description of a bipolar system with mixed

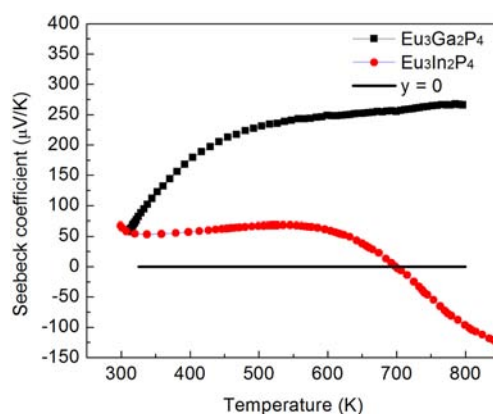


Figure 8. Seebeck coefficients of $\text{Eu}_3\text{Ga}_2\text{P}_4$ and $\text{Eu}_3\text{In}_2\text{P}_4$ as a function of temperature. Line is drawn to indicate where the Seebeck coefficient is zero.

conduction effects. Here, the Hall carrier concentration and Hall mobility, shown in Figure 7c and 7d, were calculated from a single-carrier model of the Hall effect ($n_{\text{H}} = 1/R_{\text{H}}e$) and electrical conductivity ($\sigma = n_{\text{H}}e\mu_{\text{H}}$). The Hall carrier concentration and Hall mobility data reported here are for completeness and comparison, but because the Hall coefficient is compensated by the opposing effects of both holes and electrons, the concentration and mobility of individual charge carriers cannot be definitively determined. In a two-carrier system, the expression for the Hall coefficient, R_{H} , which takes into account both holes and electrons, is given in eq 1. The single-band approximation can be used to determine the actual carrier concentration and mobility if one carrier type clearly dominates; otherwise, significant errors can be introduced (eq 1).²⁸

$$R_{\text{H}} = \frac{-n\mu_{\text{n}}^2 + p\mu_{\text{p}}^2}{e(n\mu_{\text{n}} + p\mu_{\text{p}})^2} \quad (1)$$

The Seebeck coefficient of $\text{Eu}_3\text{Ga}_2\text{P}_4$ remained relatively large and positive in the measured temperature range, varying from $\sim 60 \mu\text{V/K}$ at room temperature to $\sim 270 \mu\text{V/K}$ at 800 K, as shown in Figure 8. Likewise, the Seebeck coefficient of high zT material $\text{Yb}_{14}\text{MnSb}_{11}$ ranges from $60 \mu\text{V/K}$ at room temperature to $185 \mu\text{V/K}$ at 1275 K.⁵ The nonlinear behavior of the Seebeck coefficient with increasing temperature is indicative of both n- and p-type carriers such as those observed in $\text{Yb}_{14}\text{Mn}_{1-x}\text{Al}_x\text{Sb}_{11}$ ³¹ and $\text{Yb}_{11}\text{MSb}_9$ (M = Ga, In)²⁸ Zintl phases. The Seebeck coefficient of $\text{Eu}_3\text{In}_2\text{P}_4$ is about $60 \mu\text{V/K}$ at room temperature and slightly rises before starting to fall at 550 K, as shown in Figure 8. The expression of the Seebeck coefficient is given as a function of partial electron and hole Seebeck coefficients in two-carrier systems shown in eq 2.³²

$$S = \frac{S_{\text{e}}\sigma_{\text{e}} + S_{\text{h}}\sigma_{\text{h}}}{\sigma_{\text{e}} + \sigma_{\text{h}}} \quad (2)$$

The sign change of the Seebeck coefficient for $\text{Eu}_3\text{In}_2\text{P}_4$ suggests that the contribution from electrons is dominant at high temperatures. Similar behavior was observed for AgSbTe_2 ,³³ which showed negative values of the Hall coefficients (carrier concentration) and a positive Seebeck coefficient. The negative Hall coefficient indicates that the electrons most likely occupy high-mobility low-mass bands and dominate the Hall coefficient at all temperatures. The holes,

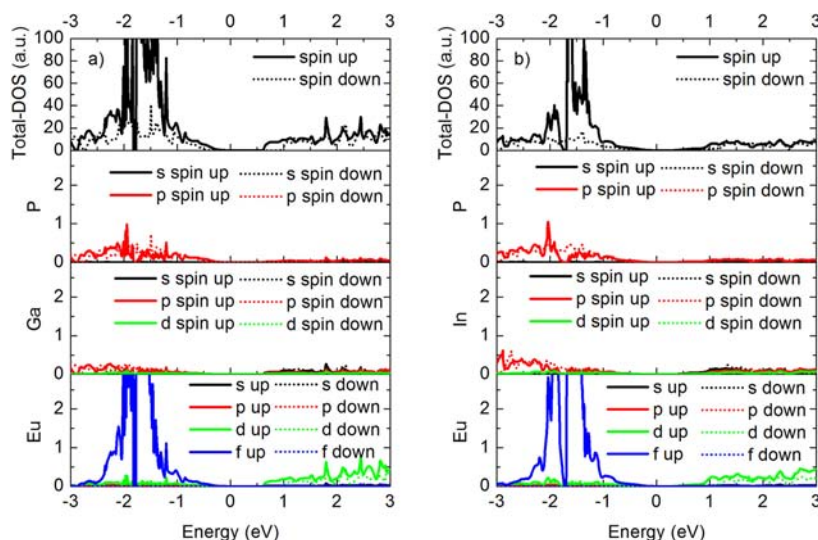


Figure 9. Density-of-states (DOS) diagrams for $\text{Eu}_3\text{Ga}_2\text{P}_4$ (a) and $\text{Eu}_3\text{In}_2\text{P}_4$ (b) based on PAW-GGA. Band gaps of $\text{Eu}_3\text{Ga}_2\text{P}_4$ and $\text{Eu}_3\text{In}_2\text{P}_4$ are 0.60 and 0.29 eV, respectively.

residing in high density of states mass bands, give a positive Seebeck coefficient of $\text{Eu}_3\text{In}_2\text{P}_4$ when the partial Seebeck coefficient dominates at low temperatures.³³ $\text{Eu}_3\text{In}_2\text{P}_4$ is a case where two distinct regions can be observed in Seebeck coefficient data. In the first region, extrinsic charge carriers excited from impurity states are dominant and the Seebeck coefficient increases with temperature as the Fermi level moves toward the middle of the band gap. In the second region, electron–hole pairs are excited across the energy gap as the temperature is further raised and the Seebeck coefficient decreases due to the opposing effects of the two types of carriers. The n-type carriers increase due to thermal excitation across a small thermal band gap. The Seebeck coefficient changes sign when the partial Seebeck coefficient of electrons starts to dominate. The maximum of the Seebeck coefficient α_{max} between these two regions can be employed to estimate the thermal band gap E_g ($\alpha_{\text{max}} \approx E_g/2eT_{\text{max}}$ where e is the charge of an electron and T_{max} is the absolute temperature at α_{max}).³⁴ A thermal band gap $E_g = 0.073$ eV can be obtained for $\text{Eu}_3\text{In}_2\text{P}_4$ based on this estimation, which is comparable to the value of 0.040(1) eV from the fitting of resistivity data. This band gap value of ~ 0.05 eV corresponds to kT at $T = 580$ K, where the Seebeck coefficient starts to decrease. Therefore, the estimated thermal band gaps from both the Seebeck coefficient and the electrical resistivity are within a reasonable range.

The figure of merit of $\text{Eu}_3\text{M}_2\text{P}_4$ is low, with zT values of ~ 0.02 and 0.01 at 800 K for $M = \text{Ga}$ and In compounds, respectively. The low zT values are mainly a result of the high electrical resistivity values due to a lack of extrinsic dopants. If proper dopants can be found to increase the charge carriers and the band-gap magnitudes are sufficiently large to prevent bipolar conduction, good thermoelectric performance may be achieved for $\text{Eu}_3\text{Ga}_2\text{P}_4$ and $\text{Eu}_3\text{In}_2\text{P}_4$ as p- and n-type materials, respectively.

Electronic Band Structure. To compare the band gaps and study the states near the Fermi level of $\text{Eu}_3\text{M}_2\text{P}_4$, the density of states (DOS) diagrams are presented in Figure 9. As can be seen from the plot, given $U_{\text{eff}} = 6.3$ eV on f states and the magnetic moment is $7 \mu_B$ for Eu, the band gap of $\text{Eu}_3\text{Ga}_2\text{P}_4$ is around 0.60 eV^{25,26} and about 0.29 eV for $\text{Eu}_3\text{In}_2\text{P}_4$. Estimation of the band gap of $\text{Eu}_3\text{Ga}_2\text{P}_4$ is in agreement with the

experimental measured 0.55 eV.¹⁶ The value of 0.29 eV for $\text{Eu}_3\text{In}_2\text{P}_4$ is smaller than the calculated band gap of $\text{Eu}_3\text{In}_2\text{P}_4$, 0.42 eV, obtained by Singh,^{35,36} which may be due to the different pseudopotentials, exchange-correlation functionals, and on-site U (or J) parameters employed. Nevertheless, the qualitative descriptions of the material features such as the semiconductor characteristic and the states distributions are similar. According to GGA(S) + U calculation, in $\text{Eu}_3\text{In}_2\text{P}_4$, the top of the valence band is dominated by f states of Eu hybridizing slightly with p states of P and the bottom of the conduction band is dominated by the d states of Eu hybridizing with s states of In, while in $\text{Eu}_3\text{Ga}_2\text{P}_4$, although f states of Eu play an important role in the top of the valence band, hybridization of p states of P is dominant. States near the band edge are contributed by spin-up components for both compounds.

In order to investigate the possible chemical bonding between Eu–P, Ga–P, and In–P, the valence charge density contour maps of $\text{Eu}_3\text{Ga}_2\text{P}_4$ and $\text{Eu}_3\text{In}_2\text{P}_4$ are presented in Figure 10. The energy scales from Fermi level to 3 eV lower

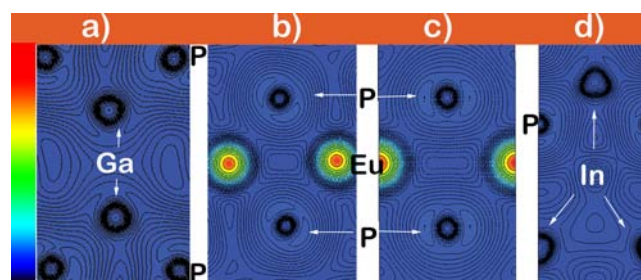


Figure 10. Valence charge density contour maps of (a) Ga–P and (b) Eu–P in $\text{Eu}_3\text{Ga}_2\text{P}_4$ and (c) Eu–P and (d) In–P in $\text{Eu}_3\text{In}_2\text{P}_4$. Relative intensities decrease from red (top) to blue (bottom).

than Fermi level, which corresponds to the $[-3 \text{ eV}, 0 \text{ eV}]$ on the DOS figure and is most relevant to chemical bond formation. The planes containing Eu–P bonds are chosen to cross the Eu atoms distant from the Ga–P/In–P tetrahedral layers in order to determine whether two-dimensional or three-dimensional electrical conductivity exists. It can be seen from

the charge contour maps that Eu, Ga, and In atoms all interact with P atoms by polar covalent bonds with a relatively strong ionic character, which indicates a possible three-dimensional electrical conductivity as previously suggested. This is also confirmed by the electronegativity differences of Eu(1.2), Ga(1.81), and In(1.78) with P(2.19) that fall into the range of polar covalent bonds.

To obtain the most appropriate fitting of the U_{eff} parameter, different U_{eff} parameters need to be tested to match with experimental parameters, such as lattice constant, etc., which may slightly alter the density of states. Also including U_{eff} on d states of Eu should change the density of states to some extent; however, U correction on both d and f states of the same element is not implemented in the present release of VASP. Therefore, we chose the correction on f states since U_{eff} is 6.3 eV for f states, which is much larger than $U_{\text{eff}} = 3.4$ eV for d states. By including the majority of the important effects, we expect the calculations to be adequate for obtaining the trend of band-gaps change and the density of states of the materials. In fact, the band gaps of $\text{Eu}_3\text{M}_2\text{P}_4$ obtained from the electronic structure calculations are comparable with the values obtained from the fittings of electrical resistivity data of single crystals.^{16,17}

CONCLUSIONS

Two rare-earth Zintl phosphides $\text{Eu}_3\text{M}_2\text{P}_4$ ($M = \text{Ga}, \text{In}$) were successfully synthesized. Refinement of the powder X-ray diffraction patterns confirms phase purity for monoclinic $\text{Eu}_3\text{Ga}_2\text{P}_4$ and orthorhombic $\text{Eu}_3\text{In}_2\text{P}_4$. $\text{Eu}_3\text{M}_2\text{P}_4$ phases exhibit high thermal stability according to the TG-DSC measurement, with no phase transitions up to 1273 K. The two phosphides show extremely low thermal conductivity (0.6 W/m·K at 700 K). $\text{Eu}_3\text{Ga}_2\text{P}_4$ shows a relatively large and positive Seebeck coefficient from ~ 60 $\mu\text{V}/\text{K}$ at room temperature to ~ 270 $\mu\text{V}/\text{K}$ at 800 K. In contrast, the Seebeck coefficient of $\text{Eu}_3\text{In}_2\text{P}_4$ turns from positive to negative values at around 550 K and reaches approximately -100 $\mu\text{V}/\text{K}$ at 800 K. As intrinsic semiconductors, both $\text{Eu}_3\text{M}_2\text{P}_4$ compounds exhibit high electrical resistivity values that decrease with increasing temperature. This is in agreement with the results of the electronic structure calculations, which provide band gaps of 0.60 and 0.29 eV for $\text{Eu}_3\text{Ga}_2\text{P}_4$ and $\text{Eu}_3\text{In}_2\text{P}_4$, respectively. The charge carrier concentration and mobility variations with temperature have also been studied. The figure of merit of $\text{Eu}_3\text{M}_2\text{P}_4$ is low, approximately 0.02 and 0.01 at 800 K for $M = \text{Ga}$ and In , respectively. Improvements of thermoelectric properties can be achieved by optimizing the carrier concentration through extrinsic doping.

ASSOCIATED CONTENT

Supporting Information

Listings of thermal diffusivity data (pdf). This material is available free of charge via the Internet at <http://pubs.acs.org>.

AUTHOR INFORMATION

Corresponding Author

*E-mail: smkauzlarich@ucdavis.edu.

Notes

The authors declare no competing financial interest.

ACKNOWLEDGMENTS

We gratefully acknowledge financial support from NSF DMR1100313, NSF/DOE Partnership CBET-1048799, and NASA Jet Propulsion Laboratory.

REFERENCES

- (1) Brian C, S. *Curr. Opin. Solid State Mater. Sci.* **1997**, *2* (3), 284–289.
- (2) Goldsmid, H. J.; Nolas, G. S. *Proceedings ICT'01. 20th International Conference on Thermoelectrics*, Beijing, China, June 2001; IEEE: Piscataway, NJ, 2001; pp 1–6.
- (3) In *CRC handbook of Thermoelectrics*; Rowe, D. M., Ed.; CRC Press: Boca Raton, FL, 1995; p 410.
- (4) Kauzlarich, S. M.; Brown, S. R.; Snyder, G. J. *Dalton Trans.* **2007**, 2099–2107.
- (5) Brown, S. R.; Kauzlarich, S. M.; Gascoin, F.; Snyder, G. J. *Chem. Mater.* **2006**, *18*, 1873–1877.
- (6) Gascoin, F.; Ottensmann, S.; Stark, D.; Haile, S. M.; Snyder, G. J. *Adv. Funct. Mater.* **2005**, *15* (11), 1860–1864.
- (7) Denoix, A.; Solaiappan, A.; Ayril, R. M.; Rouessac, F.; Tedenac, J. C. *J. Solid State Chem.* **2010**, *183* (5), 1090–1094.
- (8) Pan, L.; Qin, X. Y.; Xin, H. X.; Li, D.; Sun, J. H.; Zhang, J.; Song, C. J.; Sun, R. R. *Intermetallics* **2010**, *18* (5), 1106–1110.
- (9) Kumashiro, Y.; Hirabayashi, M.; Koshiro, T.; Okada, Y. *J. Less-Common Met.* **1988**, *143* (1–2), 159–165.
- (10) Huxtable, S. T.; Shakouri, A.; LaBounty, C.; Fan, X.; Abraham, P.; Chiu, Y. J.; Bowers, J. E.; Majumdar, A. *Microscale Thermophys. Eng.* **2000**, *4* (3), 197–203.
- (11) Kumashiro, K.; Hirata, K.; Sato, K.; Yokoyama, T.; Aisu, T.; Ikeda, T.; Minaguchi, M. In *Thermoelectric properties of boron and boron phosphide films*; Academic Press Inc: 2000; pp 26–32.
- (12) Zaikina, J. V.; Kovnir, K. A.; Sobolev, A. N.; Presniakov, I. A.; Kytin, V. G.; Kulbachinskii, V. A.; Olenev, A. V.; Lebedev, O. I.; Van Tendeloo, G.; Dikarev, E. V.; Shevelkov, A. V. *Chem. Mater.* **2008**, *20* (7), 2476–2483.
- (13) Shields, V.; Caillat, T.; Fleurial, J. P.; Zoltan, A.; Zoltan, L.; Tuchscherer, M. *Proceedings ICT'02. 21st International Conference on Thermoelectrics*, Long Beach, CA, Aug 2002; IEEE: Piscataway, NJ, 2002; pp 64–67.
- (14) Ponnambalam, V.; Lindsey, S.; Xie, W.; Thompson, D.; Drymiotis, F.; Tritt, T. M. *J. Phys. D: Appl. Phys.* **2011**, *44* (15), 155406.
- (15) Cordier, G.; Czech, E.; Jakowski, M.; Schaefer, H. *Rev. Chim. Mineral.* **1981**, *18* (1), 9–18.
- (16) Tsujii, N.; Uvarov, C. A.; Klavins, P.; Yi, T.; Kauzlarich, S. M. *Inorg. Chem.* **2012**, *51* (5), 2860–2866.
- (17) Jiang, J.; Olmstead, M. M.; Kauzlarich, S. M.; Lee, H. O.; Klavins, P.; Fisk, Z. *Inorg. Chem.* **2005**, *44* (15), 5322–5327.
- (18) Cordier, G.; Schaefer, H.; Stelter, M. Z. *Naturforsch., B: Anorg. Chem., Org. Chem.* **1986**, *41B*, 1416–19.
- (19) He, H.; Tyson, C.; Saito, M.; Bobev, S. J. *Solid State Chem.* **2012**, *188* (0), 59–65.
- (20) Goforth, A. M.; Hope, H.; Condrion, C. L.; Kauzlarich, S. M.; Jensen, N.; Klavins, P.; MaQuilon, S.; Fisk, Z. *Chem. Mater.* **2009**, *21*, 4480–4489.
- (21) Jiang, J.; Payne, A. C.; Olmstead, M. M.; Lee, H. O.; Klavins, P.; Fisk, Z.; Kauzlarich, S. M.; Hermann, R. P.; Grandjean, F.; Long, G. J. *Inorg. Chem.* **2005**, *44* (7), 2189–2197.
- (22) Rodriguez-Carvajal, J. *Newsletter* **2001**, *26*, 12–19.
- (23) Vandersande, J. W.; Wood, C.; Zoltan, A.; Whittenberger, D. *Therm. Conduct.* **1988**, *19*, 455.
- (24) Wood, C.; Zoltan, D.; Stapfer, G. *Rev. Sci. Instrum.* **1985**, *56*, 719.
- (25) Larson, P.; Lambrecht, W. R. L. *J. Phys.: Condens. Matter* **2006**, *18* (49), 11333–11345.
- (26) Horne, M.; Strange, P.; Temmerman, W. M.; Szotek, Z.; Svane, A.; Winter, H. *J. Phys.: Condens. Matter* **2004**, *16* (24), S061–S070.
- (27) Jiang, J.; Kauzlarich, S. M. *Chem. Mater.* **2006**, *18* (2), 435–441.

- (28) Yi, T.; Cox, C. A.; Toberer, E. S.; Snyder, G. J.; Kauzlarich, S. M. *Chem. Mater.* **2010**, *22*, 935–941.
- (29) Slack, G. A. The thermoelectrics of bulk materials: a history. *International Conference on Thermoelectrics*, Michigan, 2011; <http://www.ict2011.its.org/ict2011.its.org/system/files/Glen%20Slack's%20ICT%202011%20presentation.pdf>.
- (30) Androulakis, J.; Lin, C.-H.; Kong, H.-J.; Uher, C.; Wu, C.-I.; Hogan, T.; Cook, B. A.; Caillat, T.; Paraskevopoulos, K. M.; Kanatzidis, M. G. *J. Am. Chem. Soc.* **2007**, *129* (31), 9780–9788.
- (31) Toberer, E. S.; Cox, C. A.; Brown, S. R.; Ikeda, T.; May, A. F.; Kauzlarich, S. M. *Adv. Funct. Mater.* **2008**, *18*, 2795–2800.
- (32) Putley, E. H. *The Hall Effect and Semiconductor Physics*; Dover: New York, 1968.
- (33) Jovic, V.; Heremans, J. P. *Phys. Rev. B* **2008**, *77* (24), 245204.
- (34) Goldsmid, H.; Sharp, J. *J. Electron. Mater.* **1999**, *28* (7), 869–872.
- (35) Singh, N.; Schwingenschlögl, U. *Chem. Phys. Lett.* **2011**, *508* (1–3), 29–32.
- (36) Singh, N.; Pottgen, R.; Schwingenschlögl, U. *J. Appl. Phys.* **2012**, *112*, 103714.